Journal of Neuroinflammation

RESEARCH

Open Access

CD22 blockade exacerbates neuroinflammation in Neuromyelitis optica spectrum disorder

Wenjun Zhang[1†], Yali Han[1†], Huachen Huang[1†], Yue Su[2†], Honglei Ren[1], Caiyun Qi[1], Jinyi Li[1], Huaijin Yang[1], Jing Xu[1], Guoqiang Chang[1]

Abstract

Background Neuromyelitis optica spectrum disorder (NMOSD) is an autoantibody-triggered central nervous system (CNS) demyelinating disease that primarily affects the spinal cord, optic nerves and brainstem. Among the first responders to CNS injury, microglia are prominent players that drive NMOSD lesion formation. However, the key molecular switches controlling the detrimental activity of microglia in NMOSD are poorly understood. CD22 governs the activity of innate and adaptive immunity. In this study, we investigated to what extent and by what mechanisms CD22 may modulate microglial activity, neuroinflammation and CNS lesion formation.

Methods To determine the expression profile of CD22 in NMOSD, we performed single-cell sequencing and flow cytometry analysis of immune cells from human peripheral blood. We investigated the potential effects and mechanisms of CD22 blockade on microglial activity, leukocyte infiltration and CNS demyelination in a mouse model of NMOSD induced by injection of NMOSD patient serum-derived AQP4-IgG and human complement.

Results Single-cell sequencing and flow cytometry analysis revealed that CD22 was expressed in B cells, neutrophils, monocytes and microglia-derived exosomes in human peripheral blood from NMOSD patients and controls ($n=5$ per group). In a mouse model of NMOSD, CD22 was expressed in B cells, neutrophils, monocytes and microglia ($n=8$ per group). In NMOSD mice, CD22 blockade significantly increased the number of CNS lesions, astrocyte loss and demyelination, accompanied by increased inflammatory activity and phagocytosis in microglia. Furthermore, the detrimental effects of CD22 blockade were significantly alleviated in NMOSD mice subjected to depletion of microglia or Gr-1$^+$ myeloid cells, suggesting the involvement of microglia and peripheral Gr-1$^+$ myeloid cells. Additionally, CD22 blockade also led to significantly reduced phosphorylation of SYK and GSK3β in NMOSD. Notably, the detrimental effects of CD22 blockade were greatly diminished in NMOSD mice receiving the phosphorylated SYK inhibitor R406.

†Wenjun Zhang, Yali Han, Huachen Huang and Yue Su contributed equally to this work.

*Correspondence:
Qiang Liu
qliu@tmu.edu.cn
Ting Chang
changting1981@163.com

Full list of author information is available at the end of the article

Conclusions Our findings revealed a previously unrecognized role of CD22 as a key molecular switch that governs the detrimental effects of microglia and Gr-1$^+$ myeloid cells in NMOSD, which paves the way for the future design of immune therapies for NMOSD.

Graphical abstract

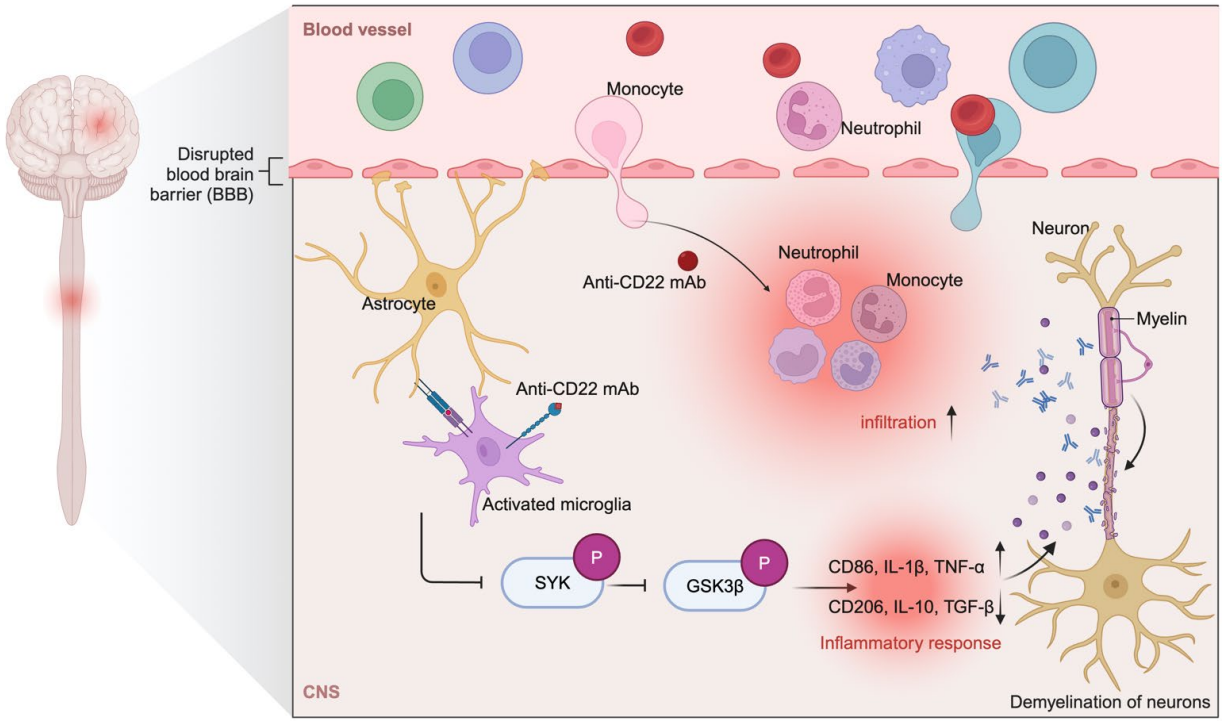

Keywords CD22, Microglia, Neuroinflammation, Neuromyelitis optica spectrum disorder, Demyelination

Introduction

Neuromyelitis optica spectrum disorder (NMOSD) is a severe disabling autoimmune and inflammatory disease of the central nervous system (CNS) that damages the optic nerve and spinal cord [1–4]. NMOSD primarily afflicts younger and middle-aged populations, resulting in high disability and increased mortality [2, 5]. NMO-IgG, i.e., antibodies against aquaporin 4 (AQP4), is a unique feature in 75% of patients with NMOSD. AQP4 is expressed mainly on astrocyte endfeet. The binding of NMO-IgG to AQP4 results in antibody-dependent cell-mediated cytotoxicity (ADCC) and complement-dependent cytotoxicity (CDC), leading to astrocyte loss, demyelination and axonal damage. The initiation of this cascade activates microglia [6, 7]. As the first responders to signals derived from astrocyte activation, microglia induce subsequent inflammatory responses [6, 8], which expedite damage to astrocytes and neuronal structures. However, the master switches that govern the detrimental activities of microglia in NMOSD remain unclear.

CD22, also known as Siglec-2, belongs to the sialic acid-binding immunoglobulin-like lectin (Siglec) family and is expressed mainly in B cells and myeloid cells, including microglia [9–11]. Although CD22 is classified as an "inhibitory receptor" in B cells that maintains a baseline level of inhibition and maintains humoral immunity, the role and function of CD22 in myeloid cells remain obscure. The distribution and function of CD22 suggest its involvement in the initiation and evolution of neuroinflammation. However, the role of CD22 in microglial activity and neuroinflammation in NMOSD remains poorly understood.

In this study, we examined the expression profile of CD22 in immune cell subsets from human peripheral blood samples collected from patients with NMOSD and control subjects. Using a mouse model of NMOSD, we assessed the expression of CD22 in immune cell subsets and determined the role of CD22 in CNS demyelination, astrocyte loss and the underlying mechanisms.

Results

Expression profile of CD22 in immune cell subsets from NMOSD patients

To determine the expression profile of CD22 in NMOSD, we performed single-cell sequencing and flow cytometry analysis of immune cells from the peripheral blood of NMOSD patients. Single-cell sequencing revealed that CD22 is expressed mainly in B cells from peripheral blood (Fig. 1A, B). Among the B-cell subsets, naïve B cells highly expressed CD22 (Fig. 1C). A decrease in CD22 expression was observed in patients with NMOSD, although the difference was not statistically significant (Fig. 1D). Flow cytometry analysis revealed that CD22 was expressed mainly in B cells, neutrophils and monocytes from peripheral blood (Fig. 1E, F). In patients with NMOSD, a significant decrease in CD22 was detected in B cells ($p=0.0022$) and monocytes ($p=0.0012$) (Fig. 1F). To assess the expression of CD22 in microglia, we isolated circulating exosomes from patients with NMOSD to assess CD22-expressing exosomes derived from microglia ($TMEM119^+CD22^+$). We observed a decrease in the number of microglia-derived $CD22^+$ exosomes in the peripheral blood of NMOSD patients compared with controls ($p=0.0012$) (Fig. 1G, H).

Expression profile of CD22 in immune cell subsets from an NMOSD mouse model

Next, we sought to assess the expression of CD22 across various immune cell types in the central nervous system (CNS) and periphery via a mouse model of NMOSD induced by intracerebral injection of human complement and AQP4-IgG, which was purified from AQP4-IgG-seropositive NMOSD patients. Flow cytometry analysis revealed that CD22 was expressed mainly by B cells, neutrophils, monocytes and microglia (Fig. 2A, B). In NMOSD mice, a decrease in CD22 expression was observed in microglia ($p=0.0064$) and CNS-infiltrating B cells ($p=0.023$) (Fig. 2C).

Overall, these findings demonstrate that CD22 is expressed mainly in B cells and myeloid cells (i.e., microglia, neutrophils and monocytes) in patients with NMOSD and in a mouse model.

CD22 blockade exacerbates NMOSD pathology in mice

To determine the potential impact of CD22 on NMOSD pathology, we utilized an anti-CD22 monoclonal antibody (anti-CD22 mAb) to block CD22 by coinjection of AQP4-IgG and human complement with anti-CD22 mAb in NMOSD mice. Demyelinating lesions were measured with T2-weighted MRI images on day 3 after NMOSD induction (Fig. 3A). We found a remarkable increase in the lesion volume of NMOSD mice receiving the anti-CD22 mAb compared with the IgG control ($p=0.0017$) (Fig. 3B). Additionally, anti-CD22 mAb treatment augmented the loss of GFAP, AQP4, and MBP expression in NMOSD mice (MBP: $p=0.0016$, GFAP: $p=0.0026$, AQP4: $p=0.0022$) (Fig. 3C, D), suggesting that CD22 blockade led to increased astrocyte loss and demyelination in NMOSD patients. Collectively, our results demonstrate that CD22 blockade exacerbates NMOSD pathology in mice.

CD22 blockade augments the inflammatory activity of microglia in NMOSD mice

To determine the effects of CD22 blockade on neuroinflammation after NMOSD, we measured microglia and CNS-infiltrating immune cells in NMOSD mouse brains via flow cytometry assessment of microglia ($CD45^+CD11b^{int}$), monocytes ($CD45^{high}CD11b^+$ $Ly6C^+$), neutrophils ($CD45^{high}CD11b^+Ly6G^+$), B cells ($CD45^{high}CD3^-CD19^+$), $CD4^+$ T cells ($CD45^{high}CD3^+CD4^+$), $CD8^+$ T cells ($CD45^{high}CD3^+CD8^+$), and natural killer (NK) cells ($CD45^{high}CD3^-NK1.1^+$) (Fig. 4A). We found that CD22 blockade led to an increase in the counts of microglia, brain-infiltrating monocytes, neutrophils and B cells in NMOSD mice (microglia: $p=0.0028$, monocytes: $p=0.0061$, neutrophils: $p=0.0011$, B cells: $p=0.048$) (Fig. 4B). To assess microglial activity, we measured the expression of CD86, CD206, IL-1β, IL-10, TGF-β and TNF-α in microglia from NMOSD mice. Flow cytometry analysis revealed that CD22 blockade led to an increase in the expression of markers of inflammatory activity (CD86, IL-1β and TNF-α) in microglia (Fig. 4C). In contrast, CD22 blockade led to a decrease in immune regulatory markers (CD206, IL-10 and TGF-β) in microglia (CD86: $p=0.012$, CD206: $p=0.044$, IL-1β: $p=0.062$, IL-10: $p=0.041$, TNF-α: $p=0.0094$, TGF-β: $p=0.013$) (Fig. 4C).

To examine the impact of CD22 blockade on microglial activity after NMOSD, we assessed the number of microglia and found that CD22 blockade led to an increase in $Iba1^+$ cells around lesions ($p=0.022$) (Fig. 4D, E). We also performed quantitative morphometric analysis of microglia on day 3 after NMOSD induction. Microglial morphology was assessed via immunofluorescence staining. Skeleton analysis revealed that following the injection of the anti-CD22 mAb, the microglial morphology changed from a ramified phenotype to a bushy phenotype (Fig. 4F). The branch lengths of microglial processes were reduced on day 3 post-NMOSD in the mice treated with the anti-CD22 mAb ($p=0.045$) (Fig. 4G). Sholl analysis further demonstrated a decrease in the complexity of microglial processes in NMOSD mice receiving the anti-CD22 mAb (Fig. 4H).

Together, these results indicate that CD22 blockade aggravates neuroinflammation in NMOSD mouse brains, suggesting a beneficial role of CD22 in controlling neuroinflammation.

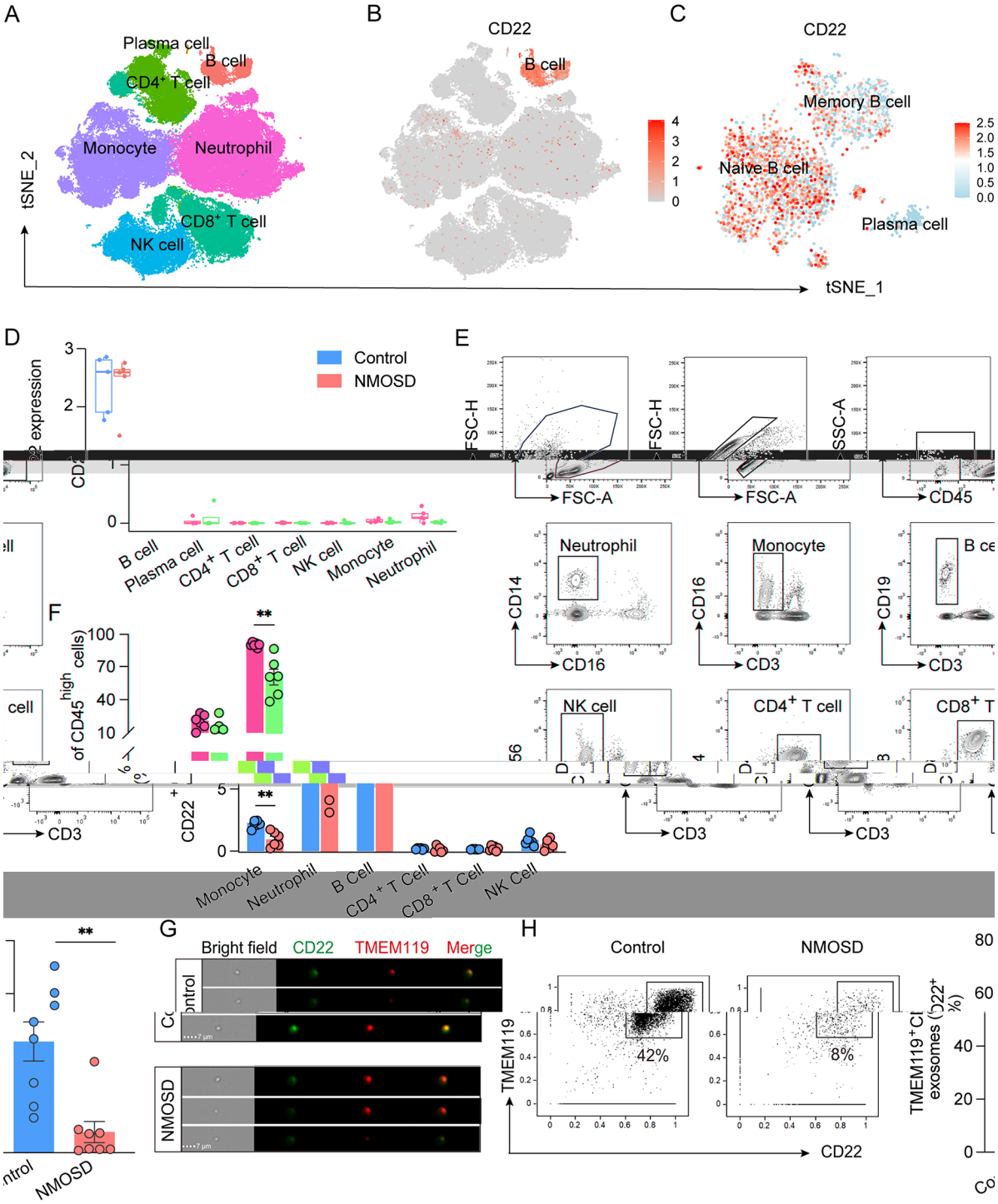

Fig. 1 Expression profile of CD22 in circulating immune cell subsets from patients with NMOSD and controls. **A** Single-cell sequencing analysis of immune cells from human peripheral blood samples from patients with NMOSD and healthy controls (total: 90,381 cells from 5 NMOSD patients and 5 controls; control: 43,985 cells; NMOSD: 46,396 cells). **B**, **C** CD22 expression profiles of B cells **B** and B-cell subsets **C** from patients with NMOSD and healthy controls; $n = 5$ per group. **D** CD22 expression profiles across various immune cell subsets in patients with NMOSD and healthy controls at the individual patient level; $n = 5$ per group. **E** Gating strategy for human circulating immune cell subsets, including neutrophils ($CD45^+CD3^-CD16^+$), monocytes ($CD45^+CD16^-CD14^+$), B cells ($CD45^+CD3^-CD19^+$), $CD4^+$ T cells ($CD45^+CD3^-CD4^+$), $CD8^+$ T cells ($CD45^+CD3^-CD8^+$) and NK cells ($CD45^+CD3^-CD56^+$). **F** Summarized bar graph showing CD22 expression in monocytes, neutrophils, B cells, $CD4^+$ T cells, $CD8^+$ T cells and NK cells; $n = 6$ per group. **G** Visualization of circulating exosomes from patients with NMOSD and controls. **H** Flow cytometry gating strategy and bar graph showing microglia-derived exosomes ($CD22^+TMEM119^+$); $n = 8$ per group. The data are presented as the mean ± SEM. $^{**}p < 0.01$

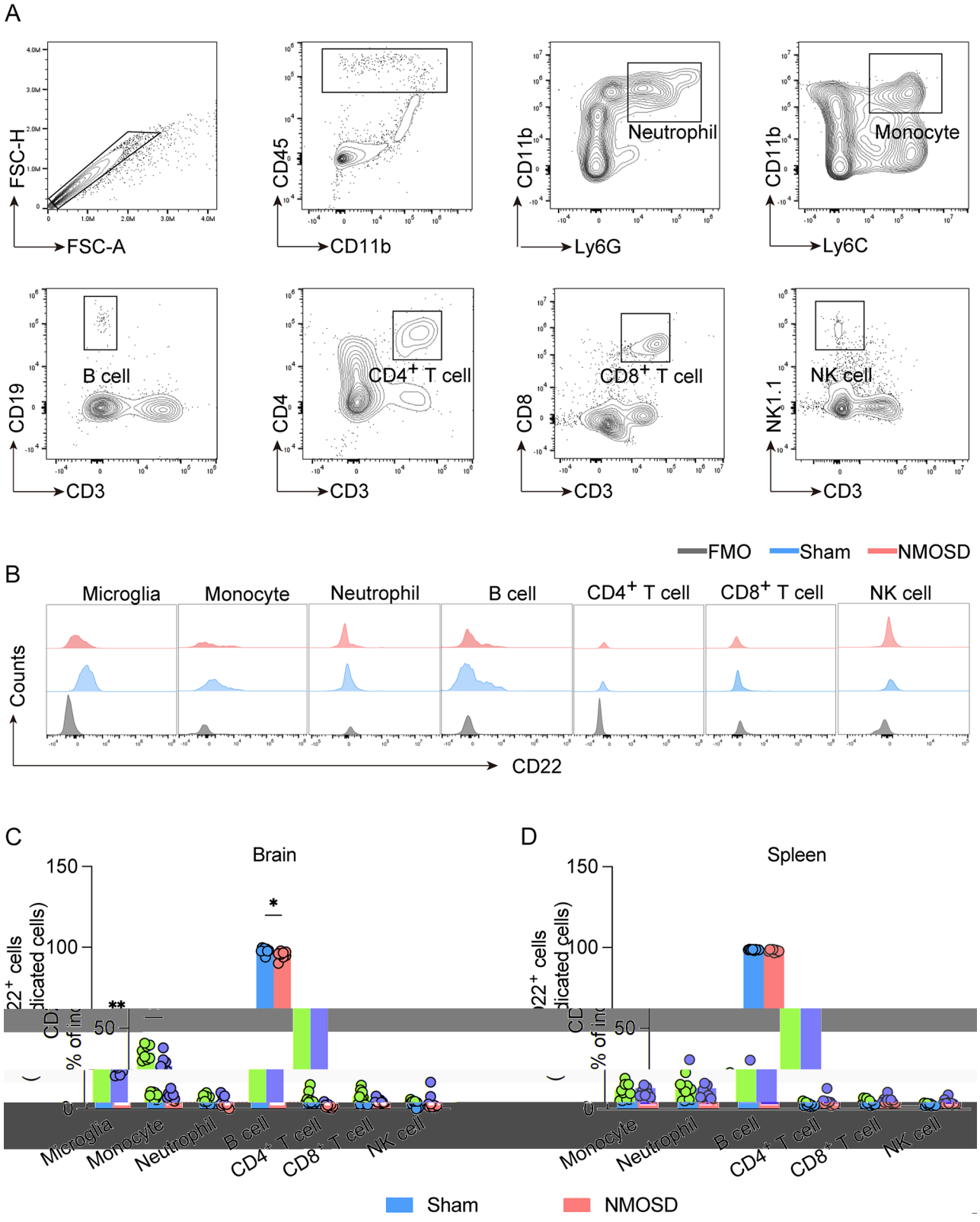

Fig. 2 CD22 expression profile in microglia and leukocytes from NMOSD mice. **A** Flow cytometry gating strategy for microglia ($CD45^{+}CD11b^{int}$), monocytes ($CD45^{high}CD11b^{+}Ly6C^{+}$), neutrophils ($CD45^{high}CD11b^{+}Ly6G^{+}$), B cells ($CD45^{high}CD3^{-}CD19^{+}$), $CD4^{+}$ T cells ($CD45^{high}CD3^{+}CD4^{+}$), $CD8^{+}$ T cells ($CD45^{high}CD3^{+}CD8^{+}$) and NK cells ($CD45^{high}CD3^{-}NK1.1^{+}$). **B** Histograms showing CD22-expressing cell subsets in sham and NMOSD mice. **C**, **D** Bar graphs showing the percentage of each cell type expressing CD22 in brain and spleen tissues from NMOSD mice; $n = 8$ per group. The data are presented as the mean ± SEM. $^{*}p < 0.05$, $^{**}p < 0.01$

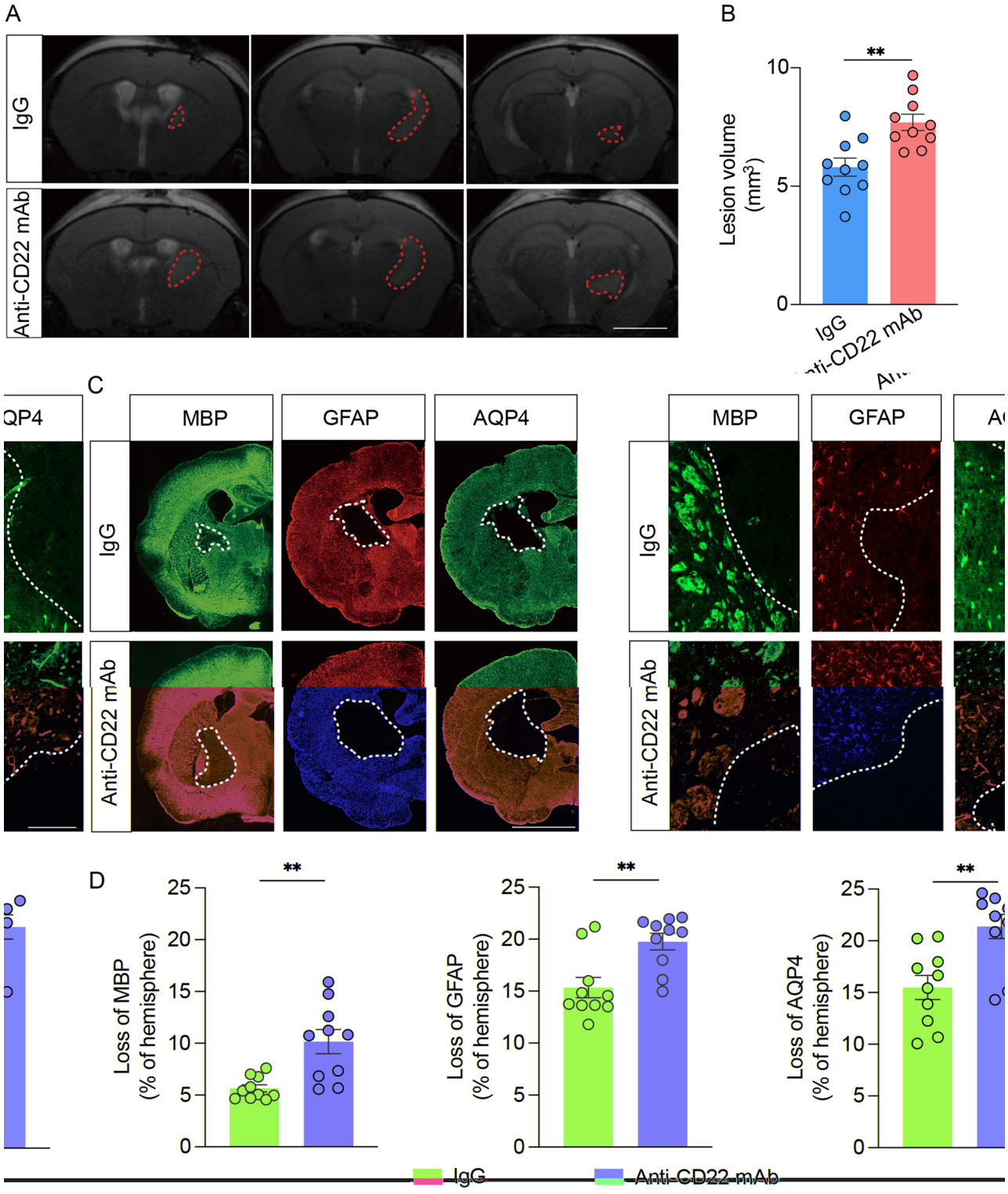

Fig. 3 CD22 blockade exacerbates NMOSD pathology in mice. **A** T2WI scans revealed demyelinating lesions in the indicated groups of NMOSD mice. The lesion areas are marked with red lines. Scale bar: 2 mm. **B** Bar graphs depicting the volume of demyelinating lesions in the indicated groups of NMOSD mice; $n = 10$ per group. **C** Immunostaining of the indicated markers (GFAP, AQP4, or MBP) in brain tissue sections from NMOSD mice receiving the anti-CD22 mAb or IgG control on day 3 after NMOSD induction. The white lines indicate areas with loss of AQP4, GFAP or MBP. Scale bar: 3,000 μm (left), 100 μm (right). **D** Bar graphs illustrating demyelination in NMOSD mice receiving anti-CD22 mAb or IgG control; $n = 10$ per group. The data are expressed as the mean ± SEM. ** $p < 0.01$

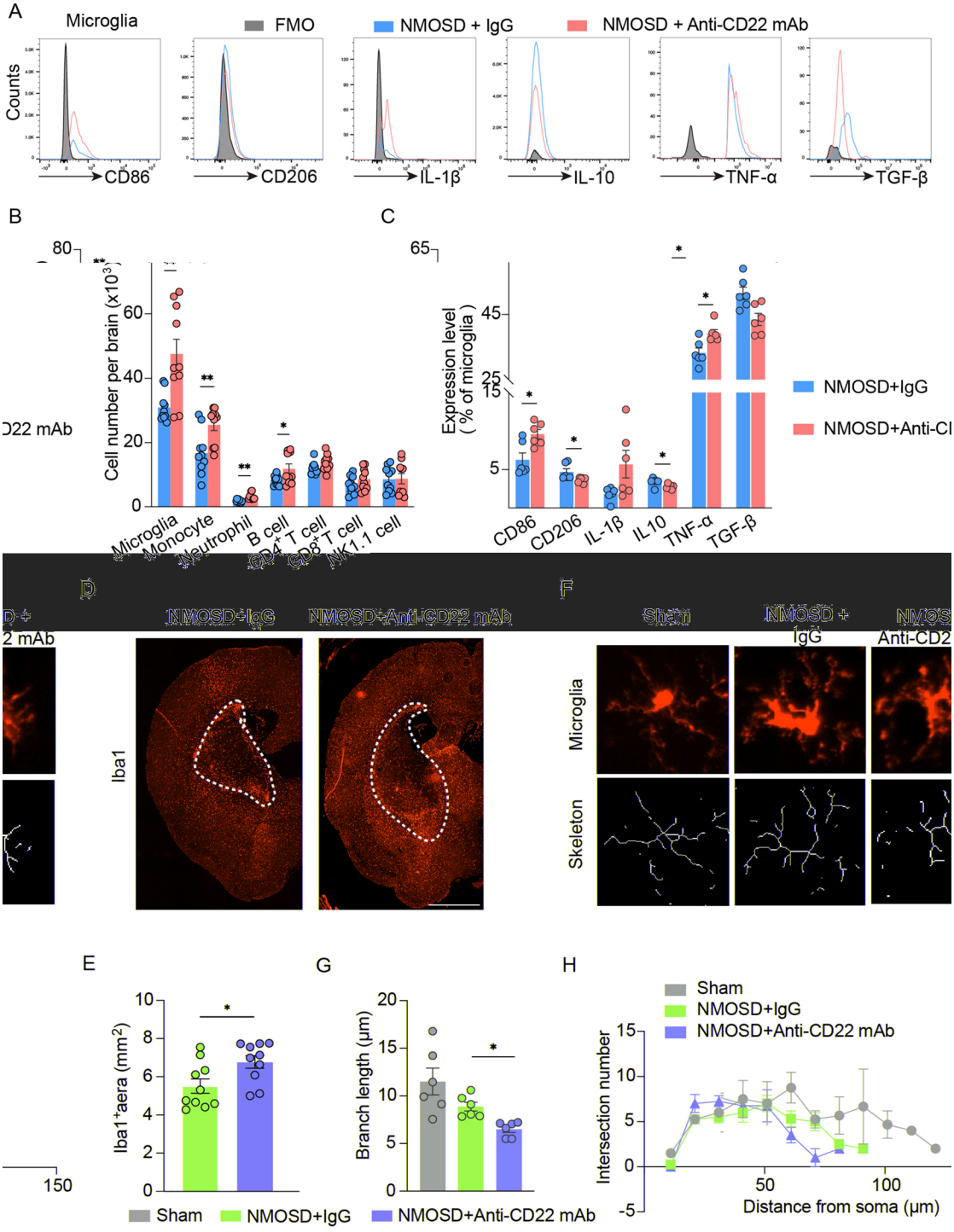

Fig. 4 CD22 blockade augments the inflammatory activity of microglia in NMOSD mice. **A** Flow cytometry gating strategy for inflammatory markers (CD86, IL-1β and TNF-α) and immune regulatory markers (CD206, IL-10 and TGF-β) in microglia. **B** Bar graph showing the effects of CD22 blockade on the counts of microglia, brain-infiltrating monocytes, neutrophils, B cells, $CD4^+$ T cells and $CD8^+$ T cells in NMOSD mice; $n = 10$ per group. **C** Flow cytometry results showing the effects of CD22 blockade on the expression of inflammatory markers (CD86, IL-1β and TNF-α) and immunoregulatory markers (CD206, IL-10 and TGF-β) in microglia from NMOSD mice; $n = 6$ per group. **D** Immunostaining showing $Iba1^+$ cells in the indicated groups. The white lines delineate the areas with an accumulation of $Iba1^+$ cells. Scale bar: 100 μm. **E** Bar graph showing that CD22 blockade enhanced the accumulation of $Iba1^+$ cells. $n = 10$ per group. **F**, **G** Skeletal analysis showing that the lengths of microglial processes were reduced on day 3 in mice treated with the anti-CD22 mAb; $n = 6$ per group. **H** Sholl analysis summarizing the results of microglial processes in NMOSD mice receiving the anti-CD22 mAb or IgG control. The data are presented as the mean ± SEM. $^*p < 0.05$, $^{**}p < 0.01$

Microglia and Gr-1+ myeloid cells contribute to exacerbated NMOSD pathology in mice receiving anti-CD22 mAb

As CD22 is expressed mainly in microglia, neutrophils, monocytes and B cells, we next examined the potential contribution of these cell types to exacerbated NMOSD pathology in mice receiving anti-CD22 mAb. For this purpose, we depleted microglia with the CSF1R inhibitor PLX5622 until the end of the experiment (Fig. 5A). In NMOSD mice receiving PLX5622, > 90% of microglia were depleted (Fig. 5B). In NMOSD mice receiving PLX5622, anti-CD22 mAb treatment did not affect the brain lesion volume (Fig. 5C, D), suggesting the involvement of microglia in the observed exacerbation of NMOSD pathology in these mice.

To test the potential involvement of peripheral myeloid cells such as monocytes and neutrophils in the detrimental impact of CD22 blockade, we used an anti-Gr-1 mAb to deplete Gr-1$^+$ myeloid cells (Fig. 6A). Flow cytometry analysis revealed that >90% of Gr-1$^+$ myeloid cells were eliminated in NMOSD mice that received the anti-Gr-1 mAb (Fig. 6B). Notably, in NMOSD mice receiving anti-Gr-1 mAb, anti-CD22 mAb treatment did not alter the brain lesion volume (Fig. 6C, D), suggesting the involvement of Gr-1$^+$ myeloid cells in the observed exacerbation of NMOSD pathology in mice receiving anti-CD22 mAb.

To investigate whether B cells contribute to the effects of CD22 blockade in NMOSD, we depleted B cells with an anti-CD20 mAb (Fig. 7A). We found that >90% of B cells were depleted in NMOSD mice receiving anti-CD20 mAb (Fig. 7B). The detrimental effects of CD22 blockade were observed in NMOSD mice receiving anti-CD20 mAb (p=0.0082) (Fig. 7C–D, Supplemental Fig. 1), suggesting that the CD22 blockade-induced exacerbation of NMOSD pathology does not involve B cells.

Collectively, these results suggest that the detrimental effects of CD22 blockade on NMOSD pathology involve microglia and Gr-1$^+$ myeloid cells.

The detrimental effects of CD22 blockade on NMOSD pathology involve SYK-GSK3β signaling

As a pivotal downstream kinase of CD22, the spleen tyrosine kinase (SYK) can switch on glycogen synthase kinase 3β (GSK3β) to modulate microglial activity [12–14]. To test whether SYK-GSK3β signaling contributes to CD22 blockade-induced exacerbation of NMOSD pathology, we used the SYK inhibitor R406 to block SYK-GSK3β signaling [15]. Consistent with previous research, we found that CD22 blockade led to reduced phosphorylation of SYK (p=0.019) and GSK3β (p=0.042) in NMOSD mice (Fig. 8B, C). T2-weighted MRI revealed that CD22 blockade no longer increased the brain lesion volume in NMOSD mice receiving R406 (Fig. 8D). Similarly, the detrimental effects of CD22 blockade on brain inflammation were diminished in NMOSD mice receiving R406 (Supplemental Fig. 2). These findings suggest that SYK-GSK3β signaling contributes to CD22 blockade-induced exacerbation of NMOSD pathology.

Discussion

This study revealed that CD22 is a master switch that governs the beneficial effects of microglia and Gr-1$^+$ myeloid cells in NMOSD pathology. As documented here, CD22 was expressed mainly in microglia, neutrophils, monocytes and B cells in patients with NMOSD and in a mouse model of NMOSD. CD22 blockade exacerbated NMOSD lesions, astrocyte loss and CNS demyelination, which was accompanied by increased inflammatory activity of microglia and CNS infiltration of peripheral myeloid cells. Notably, the detrimental effects of CD22 blockade in NMOSD pathology involve mainly microglia and Gr-1$^+$ myeloid cells but not B cells in a process involving SYK-GSK3β signaling. Collectively, these findings revealed a previously unrecognized role of CD22 in CNS inflammation and NMOSD pathology.

As the first responders to CNS injury and neuroinflammation, microglia are critical players in the control of NMOSD pathology. In NMOSD, microglia can exert either neurotoxic effects or neuroprotective effects via phagocytosis, antigen presentation and the production of various immune factors. These findings revealed that CD22 is a key molecular switch that governs microglial activity in NMOSD. The finding that microglial depletion diminishes the detrimental effects of CD22 blockade on NMOSD pathology suggests that microglia contribute to the beneficial role of CD22 in NMOSD. The activation of microglia is characterized by an amoeboid morphology, enlarged cell bodies and reduced number of branches. Indeed, we found that CD22 blockade led to an increase in the number of amoeboid microglia in NMOSD mice, which was accompanied by an increase in the expression of inflammatory markers (CD86, IL-1β and TNF-α) and reduced expression of immune regulatory markers (CD206, IL-10 and TGF-β). These findings suggest that CD22 is a key switch for the beneficial effects of microglia in NMOSD.

The expression of CD22 in Gr1$^+$ myeloid cells such as monocytes and neutrophils, along with their contribution to the detrimental effects of CD22 blockade on NMOSD pathology, suggest that CD22-expressing Gr1$^+$ myeloid cells could exert beneficial effects in NMOSD. This view is supported by previous studies showing immune regulatory effects of monocytes and neutrophils in other CNS inflammatory diseases [16–18], although the precise mechanisms underlying the benefit of CD22-expressing Gr1$^+$ myeloid cells in NMOSD remain unclear. In addition to microglia and Gr1$^+$ myeloid cells, B cells highly express CD22 in NMOSD. Although B-cell depletion did

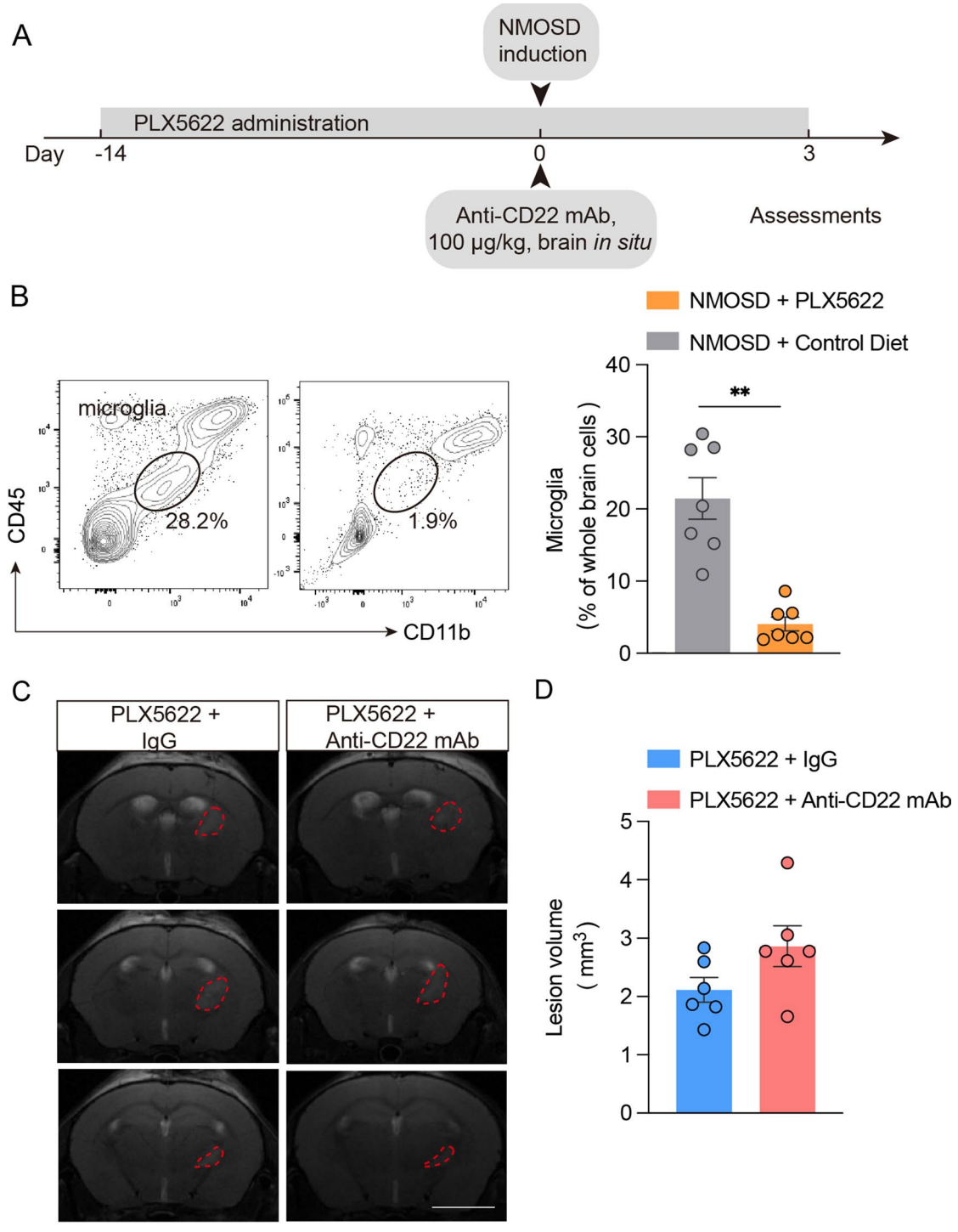

Fig. 5 Microglia contribute to exacerbated NMOSD pathology in mice receiving anti-CD22 mAb. **A** Flow chart depicting drug administration and the indicated assessment. On day 14 after microglial depletion via PLX5622, wild-type mice received intrastriatal injections of anti-CD22 mAb after NMOSD induction. **B** Assessment of microglia following PLX5622 administration; $n = 7$ per group. **C** T2WI scans showing brain lesions in the indicated groups of NMOSD mice. Red lines outline lesion areas. Scale bar: 2 mm. **D** Bar graph showing lesion volume in the indicated groups of NMOSD mice; $n = 6$ per group. The data are presented as the mean ± SEM. $^{**}p < 0.01$

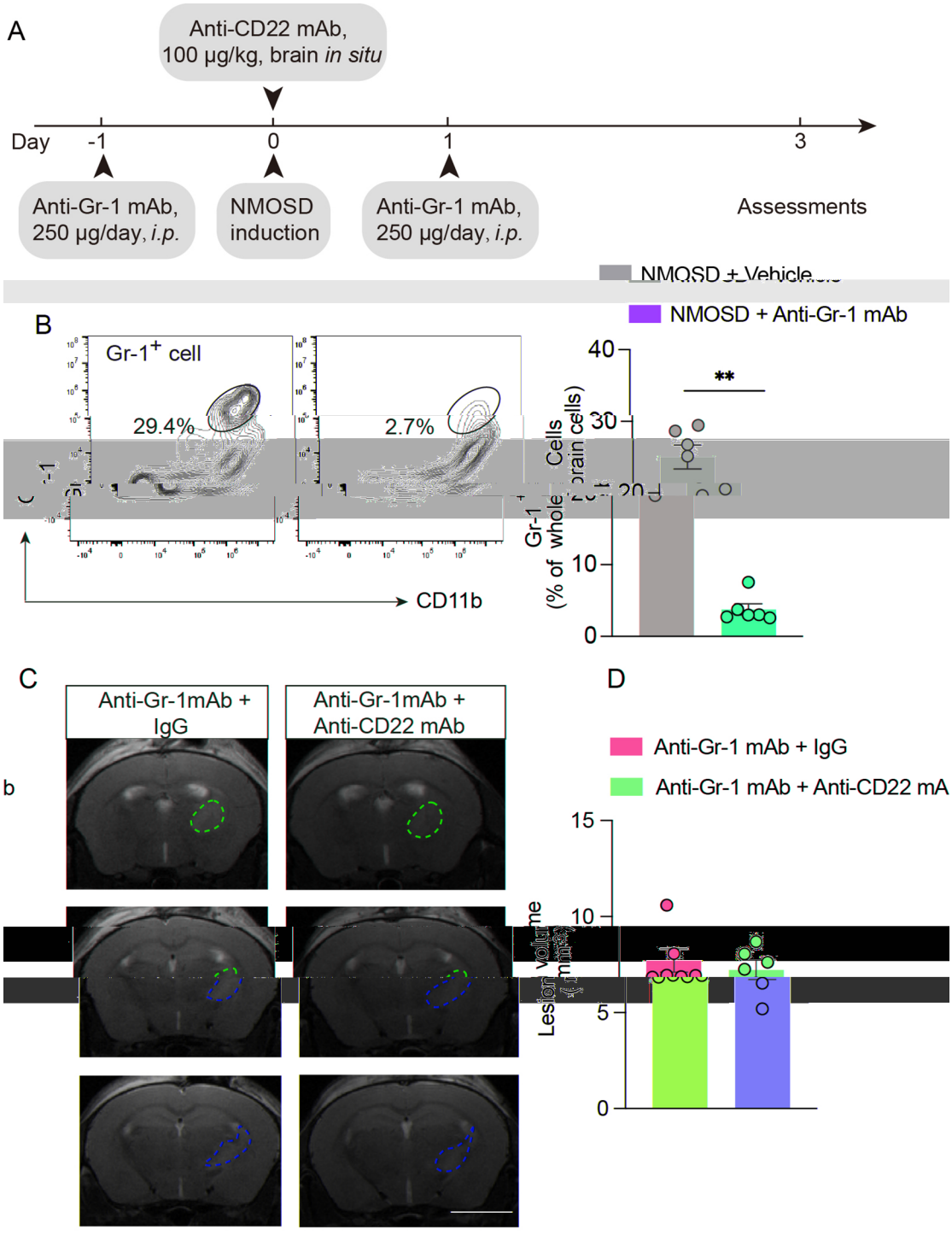

Fig. 6 Gr-1$^+$ myeloid cells contribute to exacerbating NMOSD pathology in mice receiving anti-CD22 mAb. **A** Flow chart depicting the drug administration and experimental procedures. Mice received anti-Gr-1 mAb before and one day after NMOSD induction. **B** Assessment of Gr-1$^+$ myeloid cells in mice receiving anti-Gr-1 mAb or IgG control; $n = 6$ per group. **C** T2WI scans showing brain lesions in the indicated groups of NMOSD mice. Red lines mark the lesion areas. **D** Bar graph depicting lesion volume in the indicated groups of NMOSD mice; $n = 6$ per group. The data are presented as the mean ± SEM. $^{**}p < 0.01$

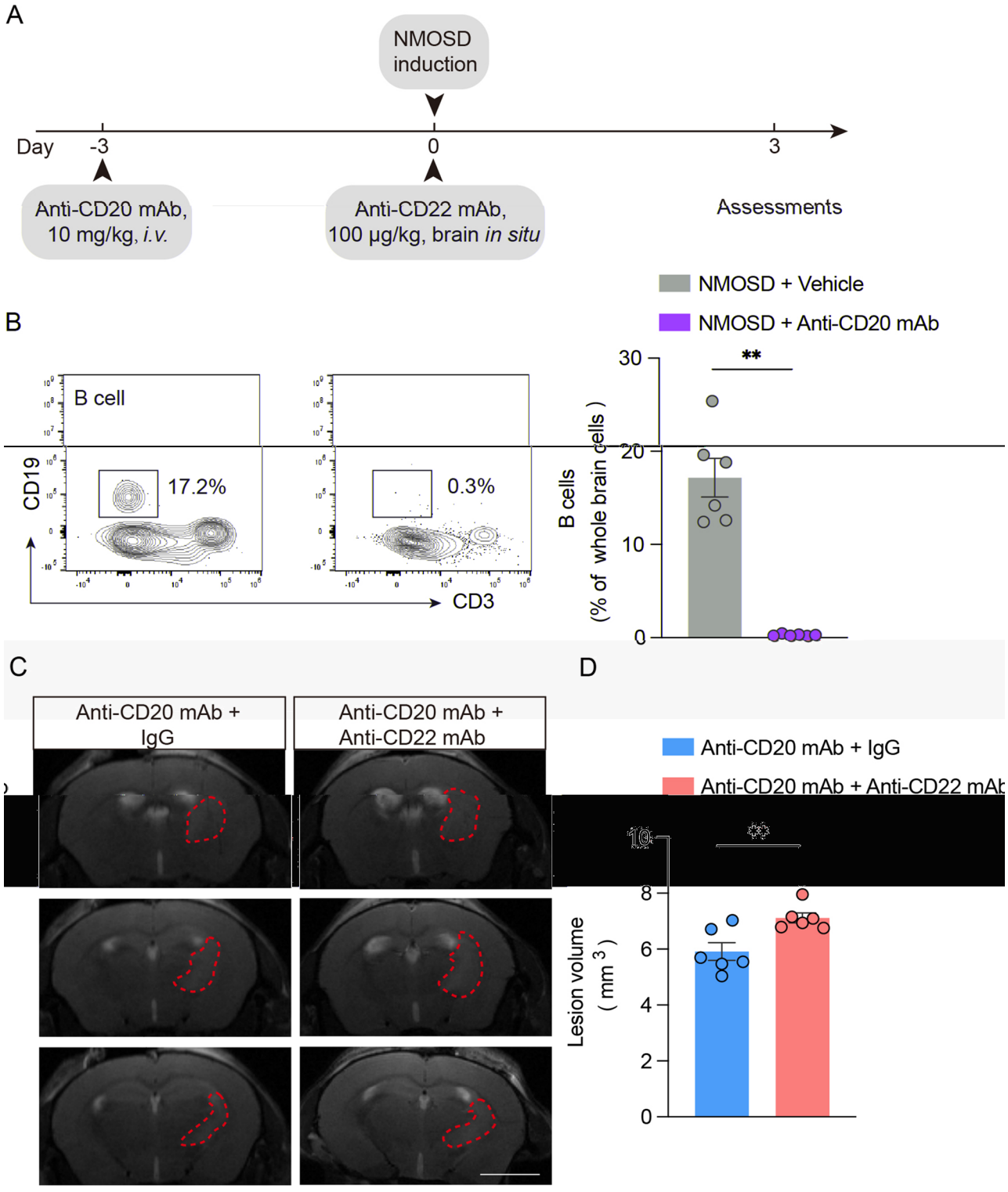

Fig. 7 CD22 blockade exacerbated NMOSD pathology in mice receiving anti-CD20 mAb. **A** Flow chart depicting the experimental procedures. The mice received anti-CD20 mAb three days prior to NMOSD induction. **B** Assessment of B cells in mice receiving anti-CD20 mAb; $n = 6$ per group. **C** T2WI scans showing brain lesions in the indicated groups of NMOSD mice. Red lines mark the lesion areas. **D** Bar graph showing lesion volume in the indicated groups of NMOSD mice; $n = 6$ per group. The data are presented as the mean ± SEM. $^{**}p < 0.01$

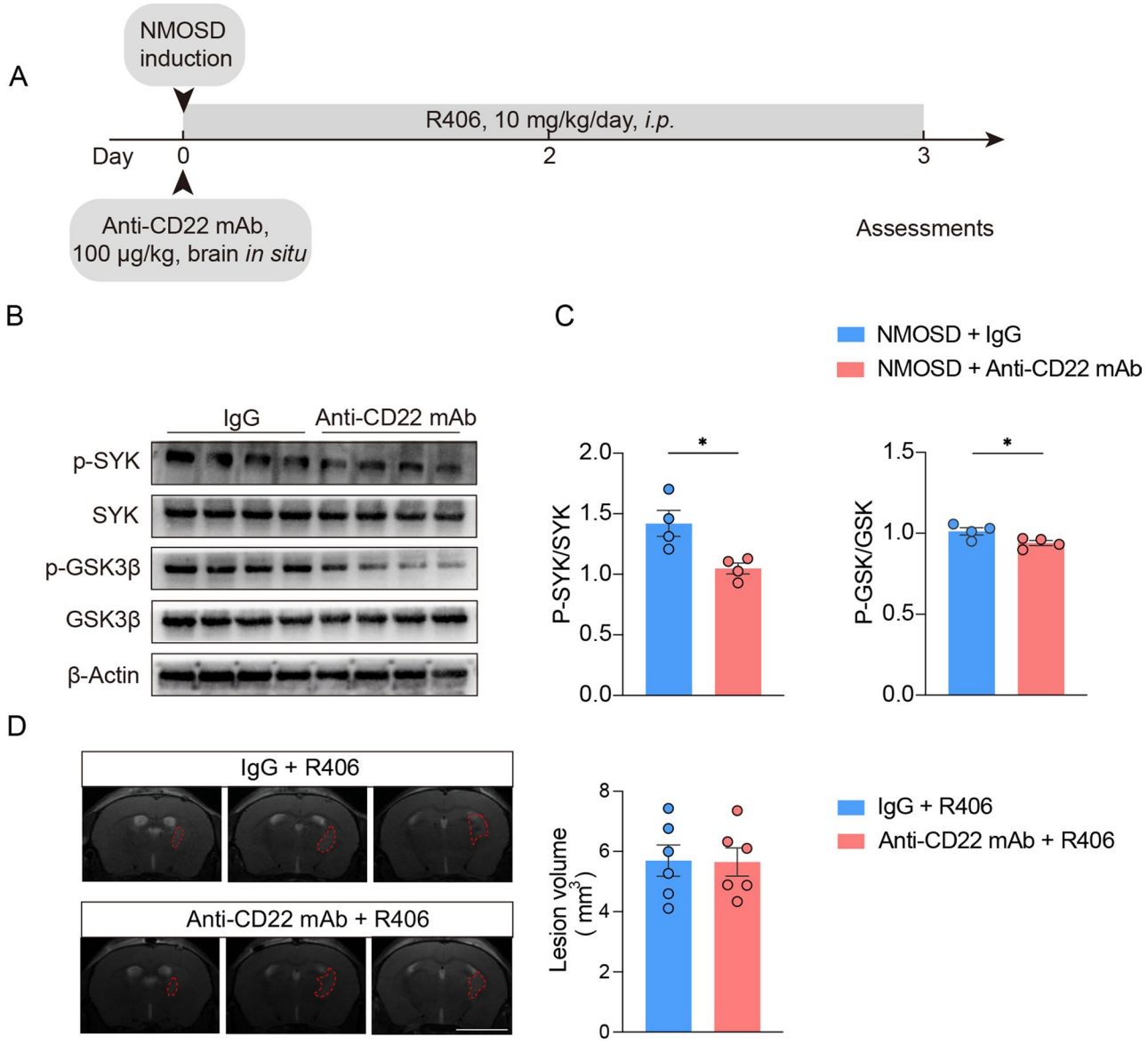

Fig. 8 The detrimental effects of CD22 blockade on NMOSD pathology involve SYK-GSK3β signaling. **A** Flow chart depicting the experimental procedures. The mice received R406 starting from the onset of modeling until they were sacrificed. **B**, **C** Assessment of the phosphorylation levels of SYK and GSK3β in the indicated groups of NMOSD mice; $n=4$ per group. **D** T2WI scans showing brain lesions in the indicated groups of NMOSD mice. Bar graph showing lesion volume in the indicated groups of NMOSD mice. Red lines mark the lesion areas; $n=6$ per group. The data are presented as the mean ± SEM. $^{*}p<0.05$

not alter NMOSD pathology in mice receiving anti-CD22 mAb, the potential effects of CD22 blockade on B-cell activity in patients with NMOSD are inadequately understood and deserve further investigation given the central role of B cells in human NMOSD.

The finding that SYK-GSK3β signaling contributes to the detrimental effects of CD22 blockade in NMOSD suggests a beneficial role of SYK-GSK3β signaling in NMOSD. Reportedly, SYK-GSK3β signaling can coordinate microglial activity and exert protective effects in neurodegenerative diseases [19–21, 22, 23]. In support of this view, we found that SYK-GSK3β signaling contributes to the benefit of CD22 in NMOSD. These findings provide a new understanding of SYK-GSK3β signaling in CNS inflammation and deserve future investigations in NMOSD and perhaps other CNS inflammatory disorders.

In contrast to NMOSD, we previously reported that CD22 blockade led to reduced neuroinflammation and brain injury in patients with intracerebral hemorrhage (ICH) [24]. This discrepancy highly likely resulted from the different causes of brain pathology in patients with ICH versus those with NMOSD. The major cause of brain injury in patients with ICH is hematoma formation along

with its mass effects. In the context of ICH, CD22 blockade augmented the phagocytosis of microglia, which is critical for hematoma clearance and the restriction of mass effects, leading to reduced neuroinflammation. In contrast, CNS autoimmunity and inflammation are the major causes of astrocyte loss and CNS demyelination in NMOSD. CD22 blockade led to increased inflammatory activity in microglia, which in turn could amplify CNS autoimmunity and inflammation, leading to increased infiltration of immune cells and exacerbating lesion volume and demyelination. Therefore, the disease-specific effects of CD22 blockade on microglial activity and CNS injury are context dependent and involve specific immune mechanisms, which should be interpreted with caution.

To restrict neuroinflammation by targeting CD22 in various brain diseases, CD22 agonists and antagonists can be used to modulate the inflammatory activity of microglia and other myeloid cell types. For example, a CD22 antagonist may benefit patients with Alzheimer's disease and ICH by increasing the phagocytosis of microglia and perhaps other myeloid cells. On the other hand, in the context of CNS autoimmune diseases such as NMOSD, CD22 agonists may reduce the activity of overactive microglia and other myeloid cells to restrict harmful neuroinflammation. Additionally, CD22 modulation may serve as a combined therapy with current treatments for various brain diseases and deserves further investigation.

Conclusion

In summary, our results demonstrate that CD22 is a protective modulator that restricts neuroinflammation and NMOSD pathology. The benefit of CD22 may result from its action on microglia and $Gr1^+$ myeloid cells in NMOSD, a process involving SYK-GSK3β signaling. These findings revealed a previously unrecognized role of CD22 in NMOSD pathology and deserve future investigations of its potential clinical implications.

Methods

Human blood samples

Patients with NMOSD ($n=15$) and healthy controls ($n=15$) were recruited from Tianjin Medical University General Hospital (Tianjin, China). Patients with NMOSD were diagnosed on the basis of the 2015 International Panel for Neuromyelitis Optica Diagnosis criteria [25]. Blood samples for flow cytometry were collected from patients during the acute phase of NMOSD. The participants in this study were matched for age and sex. Patient studies were approved by the Ethics Committees of Tianjin Medical University General Hospital.

Isolation of exosomes from human plasma

Exosomes in plasma were extracted following established protocols [26–28]. Peripheral blood from patients in the acute stage of NMOSD was collected and centrifuged at 2000 × g for 20 min, followed by additional centrifugation at 10,000 × g for 20 min to remove cell debris. The supernatant was carefully aspirated. Subsequently, the plasma was diluted with PBS, and an exosome extraction solution (Invitrogen, total exosome precipitation reagent from plasma) was added prior to 10 min of incubation at room temperature. The plasma was centrifuged again at 10,000 × g for 5 min. Thereafter, the supernatant was discarded, and the mixture was then centrifuged at 10,000 × g for 1 min. The supernatant was aspirated, leaving the precipitated exosomes at the bottom. Exosomes were resuspended in PBS and prepared for fluorescence staining for 1 h. The following antibodies were used: TMEM119 (Abcam, AF647) and CD22 (BioLegend, AF488). Exosomes were detected via an ImageStream®X MKII imaging flow cytometer (ISx, EMD Millipore, Seattle, WA, USA). Data analyses were performed via Image Data Exploration and Analysis Software (IDEAS®, Version 6.2, 2015).

Single-cell RNA sequencing

Peripheral blood samples were collected from 5 NMOSD patients and 5 healthy controls. Peripheral blood mononuclear cells were extracted and subjected to single-nucleus sequencing via the 10x Genomics platform. The following procedures were used: (1) Quantification of each gene for cells was performed via the default parameters in the Cell Ranger pipeline. The filtered gene–barcode matrix was processed via the Seurat package in R, and cells whose expression of genes was greater than 200 and whose percentage of mitochondria was less than 5% were selected for downstream analysis. (2) Data normalization (NormalizeData), identification of highly variable genes (FindVariableFeatures), standardization (ScaleData), and principal component analysis (RunPCA) were conducted via relevant functions in the Seurat package. A two-dimensional representation of overall cell populations was subsequently obtained via the t-distributed stochastic neighbor embedding (tSNE) method (RunTSNE). Further clustering (FindNeighbors, FindClusters) grouped cells with similar gene expression profiles, where the distance between cells represented the similarity between cell subgroups. (3) Cell identities were determined on the basis of the expression of subtype-specific genes for T cells (CD3D and TRAC), NK cells (KLRF1, NKG7, and KLRD1), B cells (CD19, CD79A, and CD79B), plasma cells (CD19, CD79A, TNFRSF17, and CD38), monocytes (CD14), and neutrophils (FCGR3B and NAMPT). The expression of CD22 was visualized

via the FeaturePlot and Dotplot functions in the Seurat R package.

Mice

Six- to eight-week-old C57BL/6 mice were purchased from Spafford Laboratories (Beijing, China). All the mice were housed in a pathogen-free environment with *ad libitum* access to food and water under a standardized light–dark cycle. All the mice were maintained at a standardized temperature (21 ± 1 °C) and humidity (50-60%). The mice were randomly assigned to experimental or control groups. All experimental procedures were approved by the Animal Care and Use Committees of Tianjin Neurological Institute.

Isolation of AQP4-IgG from patient serum

Serum samples were collected from AQP4-IgG seropositive NMOSD patients at Tianjin Medical University General Hospital (Tianjin, China). The serum IgG was purified according to a previously described protocol [29, 30] and diluted with Tris-buffered saline (pH = 7.0). Patient serum IgG was purified with agarose protein-A (Beyotime Biotechnology). The IgG on agarose protein-A was eluted with glycolic acid (pH = 2.5), and then, the acidic eluate was dialyzed to neutrality (pH = 7.0) in Tris-buffered saline for 8 h. The samples were concentrated in Amicon ultracentrifugal filter units (30 kDa, Merck Millipore) to a concentration of 8 mg/ml. Control IgGs were collected in the same way from healthy volunteers at a concentration of 8 mg/ml.

NMOSD model

Mice were injected with AQP4-IgG and human complement in the intraparenchyma as previously described [30, 31]. The mice were anesthetized via inhalation of 3% isoflurane and continuously inhaled 1% isoflurane to maintain anesthesia during surgery. Satisfactorily anesthetized mice were fixed on a stereotactic frame (RWD Life Science), then the scalps of the mice were sterilized, and an incision was made along the median line to fully expose the fontanel. A burr hole was made in the skull 2.5 mm to the right of the bregma. A 50-μL gas-tight glass syringe (Hamilton) attached to a 34-gauge needle was inserted into the brain parenchyma to a depth of 3 mm, and 6 μL of AQP4-IgG and 4 μL of HC were injected into the parenchymal tissue at a rate of 0.8 μL/min. After the injection was completed, surgical sutures were applied to the scalps of the mice. A small animal heating pad was used to maintain the rectal temperature at a body temperature of 37 °C during surgery. Mice that bled during surgery were excluded from the analysis. After injection, the mice were provided adequate water and food.

Drug administration in NMOSD mice

AQP4-IgG and human complement were used to induce NMOSD in mice. Sham mice received the same volume of injected IgG. Three days after surgery, the mice were sacrificed, and single brain cells were collected for flow cytometry analysis. An anti-CD22 monoclonal antibody (clone ID: CY34.1; BioXcell, West Lebanon, NH) was given to NMOSD mice via intrastriatal injection at a dose of 100 μg/mouse to deplete CD22-expressing cells [24].

To deplete microglia, the mice were fed a diet containing a CSF-1R inhibitor (PLX5622, Selleckchem, Houston, TX) [32]. Six-week-old mice were fed a diet containing PLX5622 or a control diet for two weeks before NMOSD induction. To deplete Gr-1$^+$ myeloid cells, the mice were intraperitoneally (I.P.) injected with 250 μg of anti-Ly6G/Ly6C (Gr-1) mAb (Clone ID: RB6-8C5; BioLegend, San Diego, CA) one day before and one day after NMOSD induction. To deplete B cells, an anti-CD20 mAb was administered by intravenous (I.V.) injection at a dose of 10 mg/kg three days prior to NMOSD induction. The mouse spleen tyrosine kinase (SYK) inhibitor R406 (Selleckchem, Houston, TX) was administered by intraperitoneal injection at a dose of 10 mg/kg after anti-CD22 mAb (anti-CD22 mAb) injection [33].

Magnetic resonance imaging

As previously described [34], lesion volume was quantified on day 3 after NMOSD induction using 9.4T MRI. The mice were anesthetized with 3% isoflurane and maintained at 1–2% isoflurane. A T2-weighted image scan was used to measure lesion volume. The scanning parameters were set as follows: TR = 5100 ms, effective TE = 31.71 ms, inversion time = 2506.097 ms, and slice thickness = 0.50 mm. Areas of lesions were manually outlined on each slice. Medical image processing was used to sum the lesion volumes on each slice and multiply them by the thickness of the slice to obtain the final lesion volume. The lesion volumes were calculated by two blinded investigators.

Immunostaining

Brain tissue was collected from the mice and incubated overnight at 4 °C with the following primary antibodies: anti-GFAP (1:500, Abcam), anti-AQP4 (1:200, Boster), anti-MBP (1:500, CST), and anti-Iba1 (1:500, Abcam). The tissue was then incubated with the appropriate fluorochrome-conjugated secondary antibodies: donkey anti-goat 546 (1:1000, Invitrogen) and donkey anti-rabbit 488 (1:1000, Invitrogen) at room temperature for 1.5 h. Finally, all slices were incubated with Fluoroshield mounting medium with 4'6-diamidino-2-phenylindole (DAPI) (Abcam). Images were captured via fluorescence microscopy (Biotek Cytation 5, USA) and analyzed via ImageJ software.

Flow cytometry

Peripheral blood samples were collected from NMOSD patients in the acute phase and healthy volunteers. Mononuclear cells were isolated from whole blood samples. Human blood mononuclear cells were extracted and stained with fluorescently labeled antibodies. The following antibodies were used to quantify the differential expression of CD22 on mononuclear cells: CD45, CD11b, CD3, CD4, CD14, CD8, CD16, CD56, and CD19. Mouse brain tissue was prepared as single-cell suspensions for flow-staining analysis as previously described [24]. On day 3 after NMOSD induction, the mice were satisfactorily anesthetized with 3% isoflurane and then sacrificed, and the brains were removed after perfusion with cold PBS. The brain was minced and incubated with papain and DNase I at 37 °C for 30 min on a constant-temperature shaker. Single-cell suspensions were resuspended in 1% BSA after myelin debris was removed via centrifugation in 30% Percoll (GE Healthcare Bio-Science AB, Uppsala, Sweden), followed by staining. Single cells were stimulated for 4 h in a 1x cell stimulation cocktail (BioLegend) for intracellular cytokine staining. Then, the cells were harvested and prepared for surface and intracellular staining according to the manufacturer's instructions. The following antibodies were used: CD45, CD11b, CD3, CD4, CD19, Ly6C, Ly6G, CD86, CD206, IL-10, IL-1β, TGF-β, TNF-α, and NK1.1. Simultaneously, the fluorescence minus one (FMO) control was also stained. All the antibodies were obtained from BioLegend or eBioscience. Flow cytometry data were collected on a FACS Aria III flow cytometer (BD Bioscience) and analyzed by Flow Jo version V10 (flowjo.com).

Western blots

The mice were sacrificed after anesthesia and perfused with cold PBS, and the ipsilateral hemisphere was harvested for protein extraction. Unless otherwise noted, 20 μg of total protein was separated on 8–12% acrylamide gels via SDS–PAGE. Protein was transferred to PVDF membranes (Merck KGaA, Darmstadt, Germany). After being blocked, the membranes were incubated with primary antibodies at 4 °C overnight. Primary antibodies for western blotting were diluted as follows: Syk (1:1000, Cell Signaling Technology, Danvers, MA), phospho-Syk (1:1000, Cell Signaling Technology, Danvers, MA), and β-actin (1:1000, Cell Signaling Technology, Danvers, MA). After incubation at 4 °C overnight, the PVDF membranes were incubated with species-appropriate horseradish peroxidase (HRP)-labeled secondary antibodies (1:500, Transgene Biotech, Beijing, China) for 1 h at room temperature. The protein-specific signals were detected via a Bio-Rad 721BR08844 Gel Doc Imager (Bio-Rad, Hercules, CA). The gray values of the IB bands were quantified via ImageJ software.

Statistical analysis

All the data were analyzed via GraphPad Prism 8 software (GraphPad, Inc., San Diego, CA). The experimental design was based on our previously published similar mechanistic studies [30, 34]. All the animals were randomly assigned to the treatment groups or the control groups, and all the results were analyzed by investigators who were blinded to the experimental conditions. Two-tailed unpaired t tests were used to compare two groups, and one-way analysis of variance (ANOVA) was used for comparisons of data from multiple groups. The data are expressed as the mean ± SEM. A p value < 0.05 was considered statistically significant.

Abbreviations

AQP4	Aquaporin protein-4
ADCC	Antibody dependent cell- mediated cytotoxicity
CDC	Complement -dependent cytotoxicity
CNS	Central nervous system
CSF1R	Colony stimulating factor 1 Receptor
DAPI	4'6-diamidino-2-phenylindole
GFAP	Glial fibrillary acidic protein
GSK3β	Glycogen Synthase Kinase-3β
IL	Interleukin
MBP	Myelin Basic Protein
NMOSD	Neuromyelitis optica spectrum disorder
NK cell	Natural killer cell
PBS	Phosphate Buffered Saline
PFA	Paraformaldehyde
TMEM119	Transmembrane protein119
TGF	Transforming Growth Factor
TNF	Tumor Necrosis Factor

Supplementary Information

The online version contains supplementary material available at https://doi.org/10.1186/s12974-024-03305-2.

Supplementary Material 1

Supplementary Material 2

Acknowledgements

We extend our gratitude to all the volunteers and patients who agreed to participate in this study. We also thank all the students, doctors, and nurses from the Department of Neurology, Tianjin Medical University General Hospital for their contributions to this study.

Author contributions

T.C. and Q.L. formulated the study concept. W.Z., H.H., Y.H., and Y.S. designed the studies. W.Z., Y.H., H.H., H.Y., and J.L. performed the experiments. W.Z., Y.H., H.H., Y.S., C.Q., H.R., W.Q., and J.X. analyzed all the results. W.Z., Y.H., H.H., Y.S., W.Q., G.C., Q.L., and T.C. wrote and edited the manuscript.

Funding

This study was supported in part by National Key R&D Program of China STI2030-Major Projects (2021ZD0202400), National Natural Science Foundation of China (82301522, 82225015, 82171284, 82301495, 82201498, 82372651, 82271378), Tianjin Municipal Science and Technology Bureau (22JCQNJC00500), Tianjin Municipal Education Commission (2021KJ215, 2021ZD035), National Postdoctoral Program for Innovative Talents (BX20240097), and China Postdoctoral Science Foundation (2024M750652), Tianjin Municipal Health Commission Science and Technology Project (TJWJ2023QN011).

Data availability
No datasets were generated or analysed during the current study.

Declarations

Ethics approval and consent to participate
All animal procedures were approved by the Animal Experiments Ethical Committee of Tianjin Medical University and carried out in accordance with the Revised Guide for the Care and Use of Laboratory Animals. Written informed consent for blood donation was obtained from all control subjects and NMOSD patients, in line with the local ethical committee guidelines, and the studies were conducted under Research Ethics Committee approval (IRB2022-YX-084-01).

Consent for publication
No applicable.

Competing interests
The authors declare no competing interests.

Author details
[1]Tianjin Neurological Institute, Department of Neurology, Tianjin Institute of Immunology, State Key Laboratory of Experimental Hematology, International Joint Laboratory of Ocular Diseases, Haihe Laboratory of Cell Ecosystem, Laboratory of Post-Neuroinjury Neurorepair and Regeneration in Central Nervous System Tianjin & Ministry of Education, Ministry of Education, Tianjin Medical University General Hospital, Tianjin 300052, China
[2]Department of Neurology, Tangdu Hospital, Air Force Medical University, Xi'an, Shaanxi 710038, China
[3]Department of Neurosurgery, The Affiliated Hospital of Guizhou Medical University, Guiyang, Guizhou 550001, China

Received: 11 August 2024 / Accepted: 18 November 2024
Published online: 30 November 2024

References

1. Patterson SL, Goglin SE. Neuromyelitis Optica. Rheum Dis Clin North Am. 2017;43:579–91.
2. Yang CS, Yang L, Li T, Zhang DQ, Jin WN, Li MS, Su N, Zhangning N, Liu Q, Shao ZH, et al. Responsiveness to reduced dosage of rituximab in Chinese patients with neuromyelitis optica. Neurology. 2013;81:710–3.
3. Rosenthal JF, Hoffman BM, Tyor WR. CNS inflammatory demyelinating disorders: MS, NMOSD and MOG antibody associated disease. J Investig Med. 2020;68:321–30.
4. Afzali AM, Nirschl L, Sie C, Pfaller M, Ulianov O, Hassler T, Federle C, Petrozziello E, Kalluri SR, Chen HH, et al. B cells orchestrate tolerance to the neuromyelitis optica autoantigen AQP4. Nature. 2024;627:407–15.
5. Tian DC, Li Z, Yuan M, Zhang C, Gu H, Wang Y, Shi FD. Incidence of neuromyelitis optica spectrum disorder (NMOSD) in China: a national population-based study. Lancet Reg Health West Pac. 2020;2:100021.
6. Chen T, Bosco DB, Ying Y, Tian DS, Wu LJ. The emerging role of Microglia in Neuromyelitis Optica. Front Immunol. 2021;12:616301.
7. Qin C, Chen M, Dong MH, Yang S, Zhang H, You YF, et al. Soluble TREM2 triggers microglial dysfunction in neuromyelitis optica spectrum disorders. Brain. 2024;147:163–76.
8. You YF, Chen M, Tang Y, Yu WX, Pang XW, Chu YH, Zhang H, Shang K, Deng G, Zhou LQ, et al. TREM2 deficiency inhibits microglial activation and aggravates demyelinating injury in neuromyelitis optica spectrum disorder. J Neuroinflammation. 2023;20:89.
9. Macauley MS, Crocker PR, Paulson JC. Siglec-mediated regulation of immune cell function in disease. Nat Rev Immunol. 2014;14:653–66.
10. Duan S, Paulson JC. Siglecs as Immune Cell checkpoints in Disease. Annu Rev Immunol. 2020;38:365–95.
11. Pluvinage JV, Haney MS, Smith BAH, Sun J, Iram T, Bonanno L, Li L, Lee DP, Morgens DW, Yang AC, et al. CD22 blockade restores homeostatic microglial phagocytosis in ageing brains. Nature. 2019;568:187–92.
12. Walker JA, Smith KGC. CD22: an inhibitory enigma. Immunology. 2008;123:314–25.
13. Mócsai A, Ruland J, Tybulewicz VLJ. The SYK tyrosine kinase: a crucial player in diverse biological functions. Nat Rev Immunol. 2010;10:387–402.
14. Ennerfelt H, Frost EL, Shapiro DA, Holliday C, Zengeler KE, Voithofer G, et al. SYK coordinates neuroprotective microglial responses in neurodegenerative disease. Cell. 2022;185:4135–4152.e22
15. Tang S, Yu Q, Ding C. Investigational spleen tyrosine kinase (SYK) inhibitors for the treatment of autoimmune diseases. Expert Opin Investig Drugs. 2022;31:291–303.
16. Spiteri AG, Wishart CL, Pamphlett R, Locatelli G, King NJC. Microglia and monocytes in inflammatory CNS disease: integrating phenotype and function. Acta Neuropathol. 2022;143:179–224.
17. Kanashiro A, Hiroki CH, da Fonseca DM, Birbrair A, Ferreira RG, Bassi GS, Fonseca MD, Kusuda R, Cebinelli GCM, da Silva KP, et al. The role of neutrophils in neuro-immune modulation. Pharmacol Res. 2020;151:104580.
18. Vanderbeke L, Van Mol P, Van Herck Y, De Smet F, Humblet-Baron S, Martinod K, Antoranz A, Arijs I, Boeckx B, Bosisio FM, et al. Monocyte-driven atypical cytokine storm and aberrant neutrophil activation as key mediators of COVID-19 disease severity. Nat Commun. 2021;12:4117.
19. Ennerfelt H, Frost EL, Shapiro DA, Holliday C, Zengeler KE, Voithofer G, Bolte AC, Lammert CR, Kulas JA, Ulland TK, Lukens JR. SYK coordinates neuroprotective microglial responses in neurodegenerative disease. Cell. 2022;185:4135–e41524122.
20. Wang S, Sudan R, Peng V, Zhou Y, Du S, Yuede CM, Lei T, Hou J, Cai Z, Cella M, et al. TREM2 drives microglia response to amyloid-beta via SYK-dependent and -independent pathways. Cell. 2022;185:4153–e41694119.
21. Wang S, Colonna M. The microglial immunoreceptor tyrosine-based motif-syk signaling pathway is a promising target of immunotherapy for Alzheimer's disease. Clin Transl Med. 2023;13:e1200.
22. Xiong M, Yu H, Ye T, Lanxia M. Pathogen infection in Alzheimer's disease: pathophysiology and therapeutic strategies. Ageing Neur Dis. 2023;3:1. https://doi.org/10.20517/and.2022.32.
23. Kammula SV, Tripathi S, Wang N, Dawson VL. Unraveling the tau puzzle: a review of mechanistic targets and therapeutic interventions to prevent tau pathology in Alzheimer's disease. Ageing Neur Dis. 2023;3:22. https://doi.org/10.20517/and.2023.20.
24. Ren H, Pan Y, Wang D, Hao H, Han R, Qi C, Zhang W, He W, Shi FD, Liu Q. CD22 blockade modulates microglia activity to suppress neuroinflammation following intracerebral hemorrhage. Pharmacol Res. 2023;196:106912.
25. Wingerchuk DM, Banwell B, Bennett JL, Cabre P, Carroll W, Chitnis T, de Seze J, Fujihara K, Greenberg B, Jacob A, et al. International consensus diagnostic criteria for neuromyelitis optica spectrum disorders. Neurology. 2015;85:177–89.
26. Jiao Y, Lu W, Xu P, Shi H, Chen D, Chen Y, Shi H, Ma Y. Hepatocyte-derived exosome may be as a biomarker of liver regeneration and prognostic valuation in patients with acute-on-chronic liver failure. Hepatol Int. 2021;15:957–69.
27. Mastoridis S, Bertolino GM, Whitehouse G, Dazzi F, Sanchez-Fueyo A, Martinez-Llordella M. Multiparametric analysis of circulating exosomes and other small extracellular vesicles by Advanced Imaging Flow Cytometry. Front Immunol. 2018;9:1583.
28. Liu M, Wang D, Qi C, Zou M, Song J, Li L, Xie H, Ren H, Hao H, Yang G et al. Brain ischemia causes systemic Notch1 activity in endothelial cells to drive atherosclerosis. *Immunity* 2024.
29. Saadoun S, Waters P, Bell BA, Vincent A, Verkman AS, Papadopoulos MC. Intra-cerebral injection of neuromyelitis optica immunoglobulin G and human complement produces neuromyelitis optica lesions in mice. Brain. 2010;133:349–61.
30. Kong Y, Li HD, Wang D, Gao X, Yang C, Li M, Chang T, Liu Q. Group 2 innate lymphoid cells suppress the pathology of neuromyelitis optica spectrum disorder. FASEB J. 2021;35:e21856.
31. Duan T, Verkman AS. Experimental animal models of aquaporin-4-IgG-seropositive neuromyelitis optica spectrum disorders: progress and shortcomings. Brain Pathol. 2020;30:13–25.
32. Huang Y, Xu Z, Xiong S, Sun F, Qin G, Hu G, Wang J, Zhao L, Liang YX, Wu T, et al. Repopulated microglia are solely derived from the proliferation of residual microglia after acute depletion. Nat Neurosci. 2018;21:530–40.

33. Bukong TN, Iracheta-Vellve A, Saha B, Ambade A, Satishchandran A, Gyongyosi B, Lowe P, Catalano D, Kodys K, Szabo G. Inhibition of spleen tyrosine kinase activation ameliorates inflammation, cell death, and steatosis in alcoholic liver disease. Hepatology. 2016;64:1057–71.
34. Li Z, Han J, Ren H, Ma CG, Shi FD, Liu Q, Li M. Astrocytic Interleukin-15 reduces Pathology of Neuromyelitis Optica in mice. Front Immunol. 2018;9:523.

Publisher's note